DOI:10.18057/IJASC.2025.21.3.1

STRUCTURAL PROPERTIES OF COLD-FORMED THIN-WALLED RECTANGULAR HIGH-STRENGTH STAINLESS-STEEL SPLICED TUBULAR COLUMNS UNDER AXIAL COMPRESSION AND COMPRESSION-BENDING

Jun Zhao [1], Yang Peng [2], Hao-Xuan Li [3], Xin-Xin Zhang [4] and Jun Dong [2, *]

[1] *School of Civil Engineering and Architecture, Changzhou Institute of Technology, Changzhou 213032, China*

[2] *College of Civil Engineering, Nanjing Tech University, Nanjing 211816, China*

[3] *Jiangsu Open University, Nanjing 214257, China*

[4] *Zhejiang Changneng Planning and Design Co., Ltd., Zhejiang 310030, China*

* *(Corresponding author: E-mail: dongjun@njtech.edu.cn)*

A B S T R A C T

Stainless-steel had the advantages of high strength, high corrosion resistance and easy welding, it was suitable for cold-formed thin-walled components in marine engineering. However, most cold-formed thin-walled steel components were single-limb, it had the defect of insufficient stiffness in the weak axis direction. To solve this problem, two stainless-steel lipped channels were spliced into a rectangular tube through plug welds, and an efficient cold-formed thin-walled rectangular stainless-steel spliced tubular columns was proposed. By means of splicing, the singly-symmetric cross-sections such as lipped channel sections could be transformed into doubly-symmetric cross-sections, significantly improving the axial compression performance and bending performance of the members. Three series of axial compression short column tests were carried out. The results showed that both the V-shaped stiffeners and the straight ribs played a full stiffening role in the axial compression test. Compared with the RHS-1 series components, the capacity of the RHS-2 series increased by 46.15%, the capacity of the RHS-3 series components increased by 55.38%. The finite element parameter analysis of axial compression short columns, compression-bending short columns and median long columns was carried out. The results showed that for axial compression short columns, V-shaped stiffeners and the width-thickness ratio had a great influence on failure modes. When the depth of the V-shaped stiffener was 32 mm and the angle was 90°, the section performance was optimal. When the slenderness ratio was in the range of 33.55-147.56, the overall buckling failure occurred. For compression-bending short columns and median long columns, the eccentricity ratio and the slenderness ratio had a great influence on failure modes. When the eccentricity ratio increased from 0.1 to 2.0, the ultimate compression-bending capacity decreased by 72.14% and 69.01% respectively. When the slenderness ratio was in the range of 14.81-98.73, the compression-bending stability capacity decreased significantly with the increase of the slenderness ratio. A modified calculation formula for the compression-bending capacity was proposed, with high accuracy.

A R T I C L E H I S T O R Y

Received: 15 November 2024
Revised: 31 December 2024
Accepted: 1 January 2025

K E Y W O R D S

High-strength stainless-steel;
Spliced rectangular tubular column;
Axial compression short column test;
Compression-bending;
Finite element analysis

1. Introduction

With the rapid development of marine steel structures, the corrosion problem became the greatest weakness in marine engineering [1-3]. Compared with austenitic stainless-steel, the high-strength stainless-steel not only had high strength, but also had low manufacturing costs [4-6]. Cold-formed thin-walled components could effectively improve the stability performance and capacity [7-11]. However, the cold-formed thin-walled high-strength stainless-steel columns had few research.

With the development of cold-formed thin-walled technology, the research on cold-formed thin-walled steel columns began to be widely carried out [12-16]. Generally, there were three buckling modes for cold-formed thin-walled steel axial compression columns, including local buckling failure, distortional buckling failure and overall buckling failure [17-19]. D.A. Padilla-Llano [20] analyzed the overall buckling, distortional buckling and local buckling behaviors of single-limb C-shaped steel components under cyclic loading. The results showed that under the two different loading conditions, the initial stiffness of the components had little difference. When the load was greater than the peak load, the stiffness decreased significant under the cyclic load. Y. Lu [21] conducted axial compression tests on 18 single-limb cold-formed thin-walled C-shaped steel components, providing theoretical basis for the subsequent axial compression test. H.X. Niu [22] carried out axial compression numerical simulation of components with four stiffening methods. The results showed that under the same steel consumption, the axial compression ultimate capacity of the components with V-shaped stiffeners increased most significantly. B. Young [23] conducted axial compression performance test on the "bow" shaped high-strength cold-formed thin-walled steel double-limb column. The results showed that using the direct strength method to calculate the axial compression ultimate load of the column had certain safety. Reyes [24] studied the box-section axial compression components of welded double-limb C-shaped cold-formed thin-walled steel. The results showed that when calculating its capacity using the specification AISI S100-2007, the slenderness ratio of the components needed to be corrected compared with median long columns. I. Georgieva [25] conducted compression-bending test on double-limb Z-shaped section columns. The results showed that when the slenderness ratio was large, out-of-plane instability would occur, and the overall initial defects had a great influence on the ultimate capacity. J. Zhang [26] conducted axial compression test on I-shaped section columns formed by two web-stiffened C-shaped steel, and proposed four models for solving and calculating the critical buckling load of the section. F. Liao [27] conducted axial compression test on short columns composed of C-shaped steel and U-shaped steel through self-tapping bolts. The results showed that the short columns all suffered from local buckling and distortional buckling failure. In the current research, most of the cold-formed thin-walled components were formed by connecting two or more single-limb components through bolts or welding, while no experts conducted research on welded high-strength stainless-steel columns.

This paper proposed a cold-formed thin-walled rectangular high-strength stainless-steel spliced tubular columns. Experiments of axial compression short columns, finite element analysis of axial compression of short columns, compression-bending short and median long columns were carried out. Key parameters that affect the structural performance was studied, and the calculation formula for the ultimate capacity of compression-bending columns was proposed.

2. Axial compression test of short columns

2.1. Design and fabrication of specimens

The duplex stainless-steel had higher yield strength, lower strain strengthening coefficient and stronger corrosion resistance than austenitic stainless-steel, and the material properties were as shown in reference [28]. The axial compression short column specimens in the experiment were shown in Fig.1.

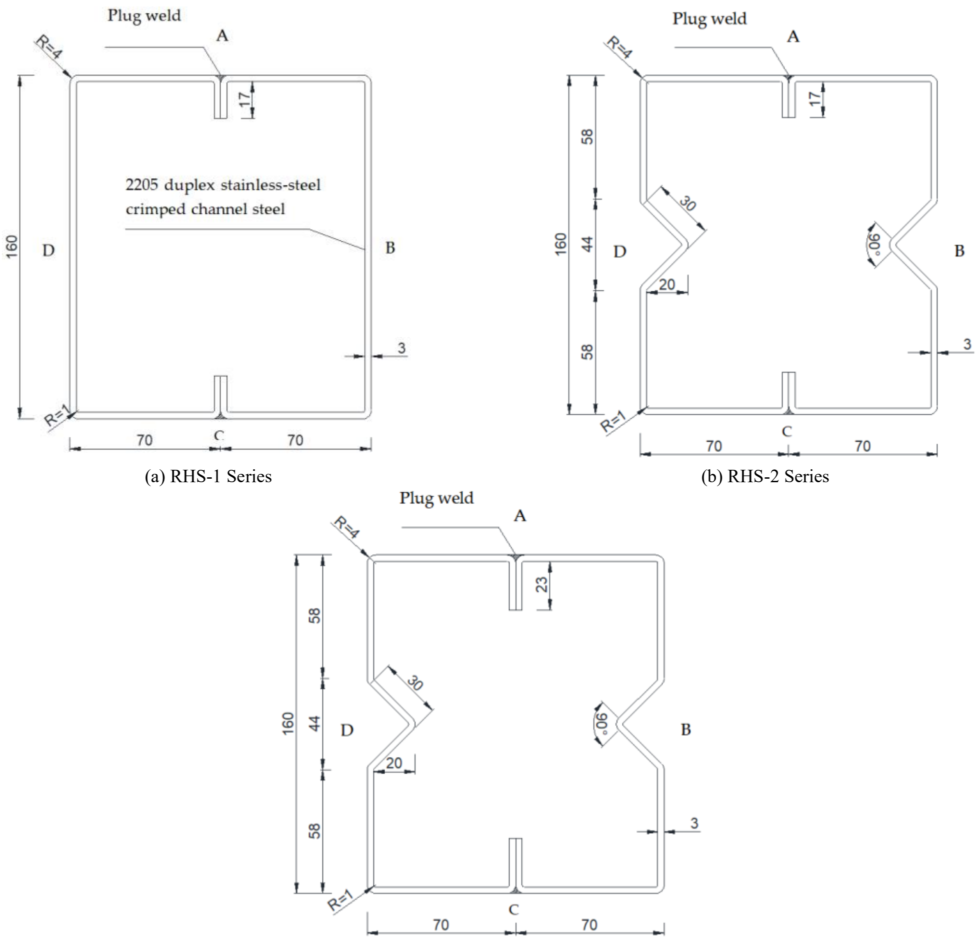

(a) RHS-1 Series (b) RHS-2 Series

(c) RHS-3 Series

Fig. 1 Detailed dimensions of components

Fig. 2 Axial compression short columns

The specimens could be divided into three groups, namely RHS-1, RHS-2, and RHS-3. The thickness of the plate was 3mm, and the length of the short column was 3 times the length of the web of the lipped channel steel, that is, 480mm. The lipped length of the RHS-3 series was 26mm. The same metal and the same technological equipment were used to manufacture a total of 9 components. The fabricated components were shown in Fig.2.

Due to the limitations of the manufacturing process, there were differences between the actual components and the design dimensions. The actual dimensions were shown in Table 1. To accurately obtain the specific detailed dimensions of the test components, the average value of the three measurement results were taken as the actual dimension of the component to avoid accidental errors during the measurement process. Through defect measurement, it was found that the initial geometric defects of the component along the length direction were much smaller than those caused by the protrusions on the weld edges, and the defect amplitude did not exceed 1 mm. Therefore, the initial geometric defects along the length direction did not affect the axial compression performance of the component.

Table 1
Measured dimensions of the components

Specimen number	H(mm)	B(mm)	a(mm)	t(mm)	Length of the V-shaped stiffeners (mm)	L (mm)
RHS-1-1	162.0	139.0	20	2.97	-	479.5
RHS-1-2	162.5	139.0	20	3.02	-	479.0
RHS-1-3	162.0	139.0	20	3.00	-	479.0
RHS-2-1	164.0	142.0	20	3.04	30	479.0
RHS-2-2	164.0	141.5	20	3.00	30	479.5
RHS-2-3	164.5	142.0	20	3.02	30	479.0
RHS-3-1	163.5	143.0	26	2.95	30	479.0
RHS-3-2	162.0	143.0	26	2.98	30	479.0
RHS-3-3	164.0	142.5	26	2.98	30	479.5

2.2. Test equipment and loading test scheme

2.2.1. Test preparation

The specimen was divided into square meshes at intervals of 30mm along the length direction to facilitate the observation and measurement of the deformation of the plate during the test process. For axial compression short columns, the most likely position for its local buckling was in the middle of the component. Displacement meters were set in the direction perpendicular to the plate at the middle section. A total of 3 displacement meters were set at the middle section of the RHS-1 series component, of which one displacement meter was arranged in the middle of the long side, and one displacement meter was arranged in the middle of the two sub-plates on the short side respectively. The RHS-2 and RHS-3 series were similar, and the displacement meters were all arranged in the middle of the sub-plates on the long side and the short side. The RHS-1 series components pasted 3 strain gauges at the middle section and the sections at B/2 from the ends at the upper and lower parts, and a total of 9 strain gauges were pasted on the entire component. The RHS-2 series components pasted 4 strain gauges at the middle section and the sections 80mm from the ends at the upper and lower parts, and a total of 12 strain gauges were pasted on the entire component. The RHS-3 series components pasted 4 strain gauges at the middle section and the sections at B/2 from the ends at the upper and lower parts, and a total of 12 strain gauges were pasted on the entire component.

2.2.2. Loading equipment and loading system

The loading equipment was a 1000T microcomputer-controlled electro-hydraulic servo pressure-shear testing machine, and the test device is shown in Fig.3. The short column components were arranged in the center of the loading platform through the end plates welded at both ends, and the load was transmitted through the end plates. The minimum displacement control speed was 0.5mm/min. The test process was displacement-controlled loading, and the loading process was continuous. The loading process could be divided into three stages. The first stage: The test system was debugged through preloading. The loading speed was 0.05mm/s (3mm/min) to 5kN to make the end plate and the test platform closely connected, and then the load was reduced to 0kN, that is, the load and displacement data were cleared, and then the readings of the strain gauge and the displacement meter were cleared. The second stage: The formal loading stage, the testing machine was controlled to move downward at a speed of 0.01mm/s (0.6mm/min), until the capacity of the component reached the peak. The third stage: The post-loading stage, when the load reached 80% of the estimated load, the moving speed was changed, and the loading was carried out at a speed of 0.05mm/s (3mm/min) to make the capacity of the component reach the ultimate capacity, and the component was damaged. Until the axial compression capacity dropped to about 80% of the peak load, the loading was stopped and the test ended.

Fig. 3 Loading equipment

2.3. Test results and analysis

2.3.1. Test process and main phenomena

As the load increased, the intervals of the "click-click" sounded emitted by the components gradually became longer, and gradually accompanied by small concave-convex local buckling of the components. When local buckling first occurred, the buckling shape was symmetrically distributed. As the load increased, the buckling half-wave gradually increased. When the ultimate load was reached, the buckling deformation of the plates expanded faster and the deformation degree was more obvious. The typical failure states of different series of components were shown in Fig.8. It could be seen no damage occurred at the weld position and the end of the component, the strength of the plug weld was sufficient, and the end restraint was sufficient. One half-wave buckling occurred on the long side of the RHS-1 component, and one half-wave buckling occurred on the short side. One half-wave buckling occurred in each of the two sub-plates on the long side of the RHS-2 component, and one half-wave buckling occurred in the middle of the short side. One half-wave buckling occurred in each of the two sub-plates on the long side of the RHS-3 component, and two half-waves buckling occurred on the upper part of the short side.

The failure modes were in line with the main objectives of component design. By comparing the members of the RHS-1 series with those of the RHS-2 series, it was found that the V-shaped stiffeners with a side length of 20 mm had sufficient stiffness to divide the lipped channel web members into two sub-plates. These two sub-plates buckled similarly to stiffened plates respectively. When comparing the members of the RHS-2 series with those of the RHS-3 series, by increasing the length of the lips, the height of the straight ribs on the short side of cold-formed thin-walled members formed by the lips was increased, so that the stiffness of the straight lips met the minimum stiffness requirement for intermediate stiffeners. However, since the straight ribs on the short side were connected by one-side plug welds through the lips, although the stiffness of the straight ribs formed by the two lips met the requirements, the width-thickness ratio exceeded the minimum width-thickness ratio limit for plates without local buckling. But because there was a certain margin in the code's limitation on the width-thickness ratio, the width-thickness ratio of the 26-mm lips in this paper only slightly exceeded the limit, and the lips did not buckle preferentially during the actual test process.

2.3.2. Test data and analysis

The comparison of the axial displacement-load curves of 9 components was shown in Fig.4. As the load gradually increased, the gap between the component section and the indenter gradually disappeared, and the component gradually transformed into full-section compression. The elastic modulus of the component gradually increased and stabilized, which was manifested in the curve as a linear increase in load with displacement. As the load increased further, the component undergone concave and convex deformation, the slope of the curve decreased and became negative, and the load began to decrease after reaching its peak load.

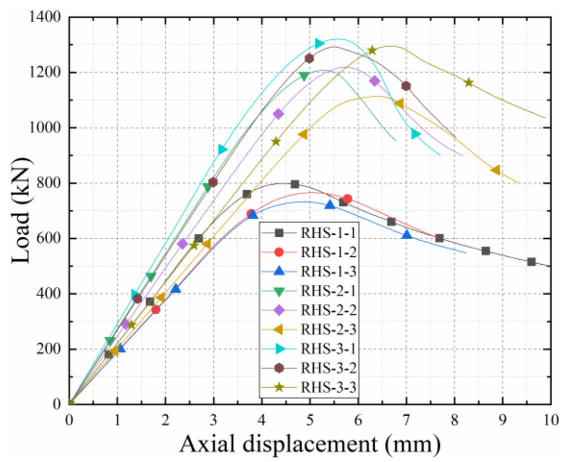

Fig. 4 Comparison of axial displacement-load curves

A displacement meter was installed in the middle of the component to record the variation of the lateral displacement at the measuring point in the middle of the component with the load during the axial compression process. The curves of lateral displacement-load of three series components were shown in Fig.5. It could be found that for the series of RHS-1 components, a relatively obvious lateral displacement occurred on surface B at around 300 kN, and local buckling occurred. The local buckling on surface B occurred earlier than that on surface C. For the series of RHS-2 components, a relatively obvious lateral displacement occurred on surface C at around 900 kN, indicating local buckling. The local buckling on surface C happened earlier than that on surface B. For the series of RHS-3 components, a relatively obvious lateral displacement occurred on surface C at around 1150 kN, meaning local buckling occurred. The local buckling on surface C occurred earlier than that on surface B. This thus proved that the installation of V-shaped stiffeners improved the local stability performance of the long sides of the spliced tubular columns, causing the location of local buckling to shift from the long sides to the short sides. The optimization of the flange length further enhanced the local stability performance of the short sides of the built-up members.

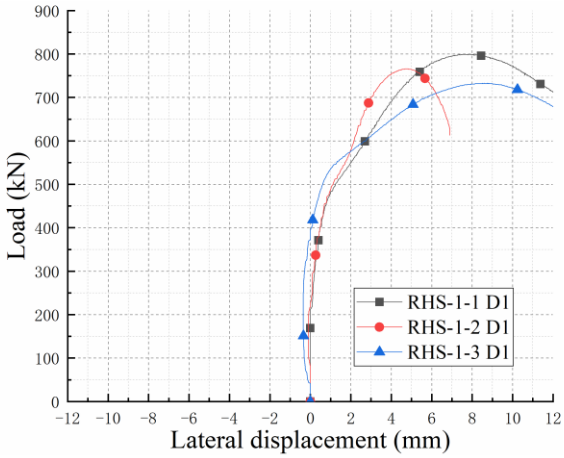

(a) Surface B of RHS-1 series components

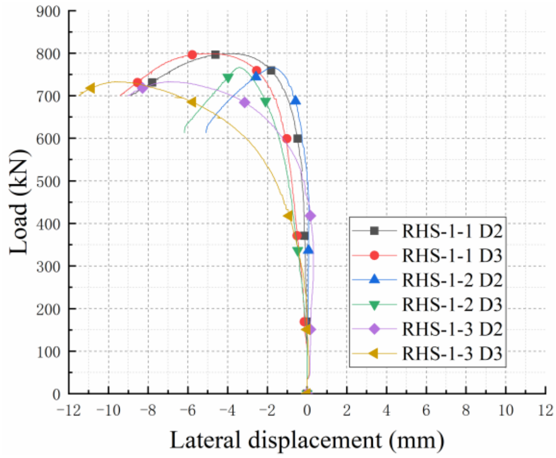

(b) Surface C of RHS-1 series components

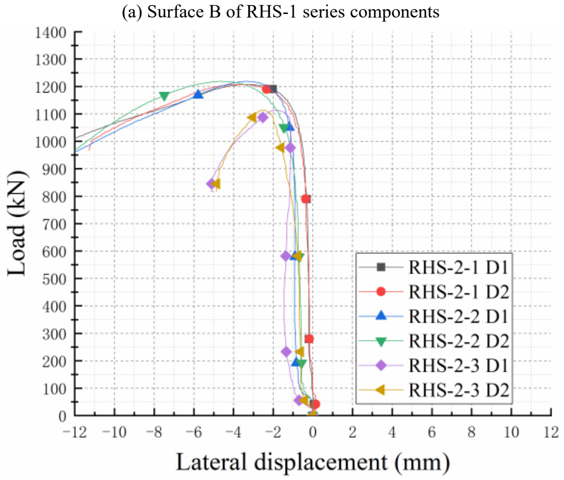

(c) Surface B of RHS-2 series components

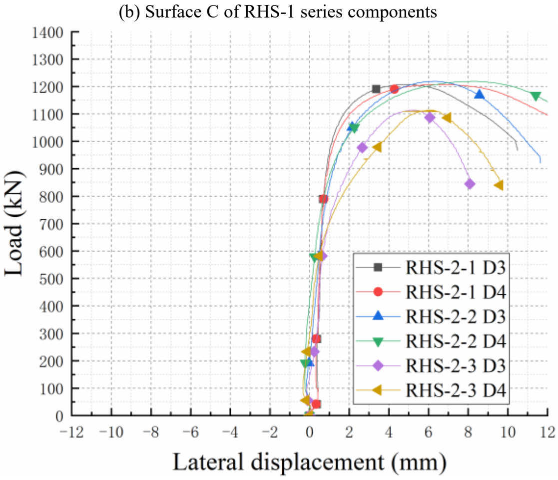

(d) Surface C of RHS-2 series components

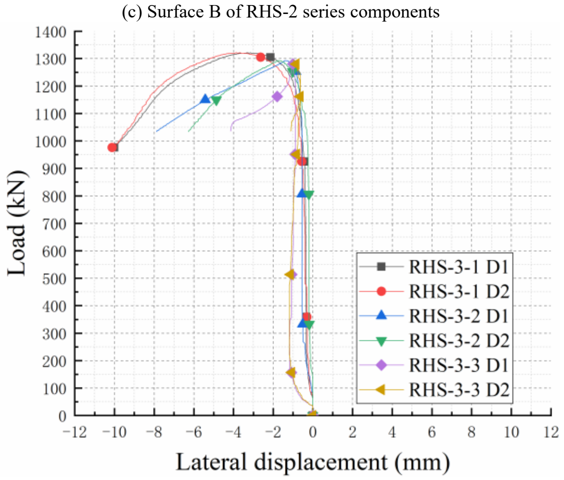

(e) Surface B of RHS-3 series components

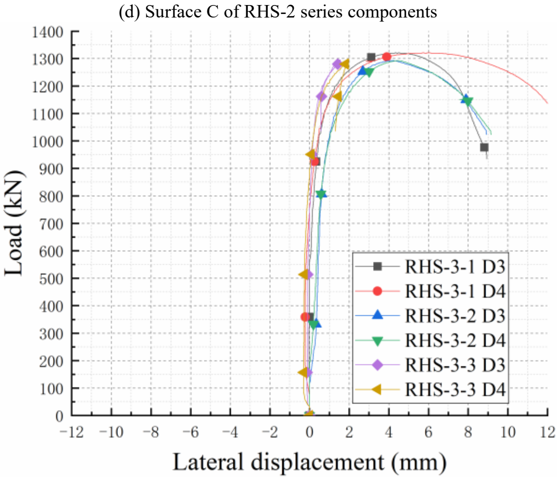

(f) Surface C of RHS-3 series components

Fig. 5 Load-lateral displacement curve of different series of components

Table 2
Mechanical properties of axial compression specimens

Specimens	Section form	Section area (mm^2)	Ultimate capacity (kN)	Extreme displacement （mm）	Ultimate strength (MPa)	$\frac{N_u}{A\sigma_{0.2}}$	Failure mode
RHS-1-1	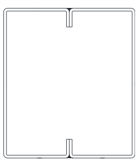		799	4.34	408.49	0.68	
RHS-1-2		1955.98	765	4.98	391.11	0.65	Local buckling; A half-wave on the long side; A half-wave on the short side
RHS-1-3			734	4.84	374.26	0.62	
	Average value		766	4.72	391.62	0.65	

RHS-2-1			1207	5.22	586.59	0.97	
RHS-2-2	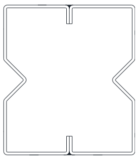	2057.67	1219	5.72	592.42	0.98	Local buckling; Two half-waves on the long side; A half-wave on the short side
RHS-2-3			1113	6.28	540.90	0.90	
	Average value		1180	5.74	573.30	0.95	
RHS-3-1			1321	5.55	620.29	1.03	
RHS-3-2	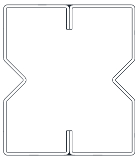	2129.65	1292	5.48	606.67	1.00	Local buckling; Two half-waves on the long side; Two half-waves on the short side
RHS-3-3			1295	6.62	608.08	1.01	
	Average value		1303	5.88	611.68	1.01	

2.3.3. Results of the test

Analyzed the axial displacement-load curve, the mechanical properties such as the initial elastic modulus and ultimate capacity of the components were obtained, as shown in Table 2.

For the RHS-1 series components, the capacity was about 766 kN. The capacity of the RHS-2 series components reached 1180 kN. The capacity of the RHS-3 series components was about 1303 kN. The bearing performance of the RHS-2 series components was improved by about 46.15% compared with the RHS-1 series components, and the capacity of the RHS-3 series components was improved by about 55.38% compared with the RHS-1 series components. The method of setting V-shaped stiffeners at the web of the stainless-steel lipped channel and extending the length of the lipped part could effectively improve the bearing performance.

3. Finite element modeling and validation

3.1. Establishment of the FEM

For the short column, the mesh size was selected as 10mm×10mm, while for the median-long column, since its model was simple and regular, its mesh size was also selected as 10mm×10mm. For the welded end plates, the mesh size was selected as 20mm×20mm. The mesh division schematic diagram of short columns was shown in Fig.6. For the contact area at the lipped joint, the normal behavior adopted the surface-to-surface hard contact. The tangential behavior adopted the isotropic friction analysis, in which the anti-slip coefficient was taken as 0.25. As for the welding at the splicing of the components, the binding (Tie) was used to constrain all degrees of freedom. Boundary conditions and loading diagram was shown in Fig.7.

3.2. Verification of the FEM

The final failure modes of the three series of RHS-1, RHS-2 and RHS-3 short columns were all local buckling. The finite element simulation results were in good agreement with the test results, and the comparison results were shown in Fig.8.

The load-axial displacement curves of the three series of short columns were shown in Fig.9. The load-displacement curves of the short columns obtained by FEM were in good agreement with the test results.

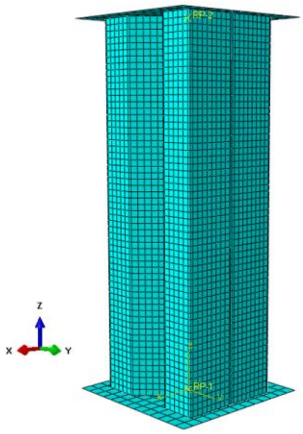

Fig. 6 Model grid division diagram

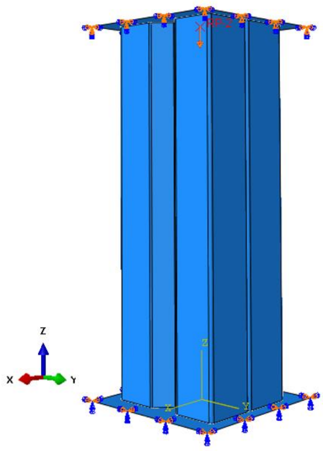

Fig. 7 Boundary conditions and loading diagram

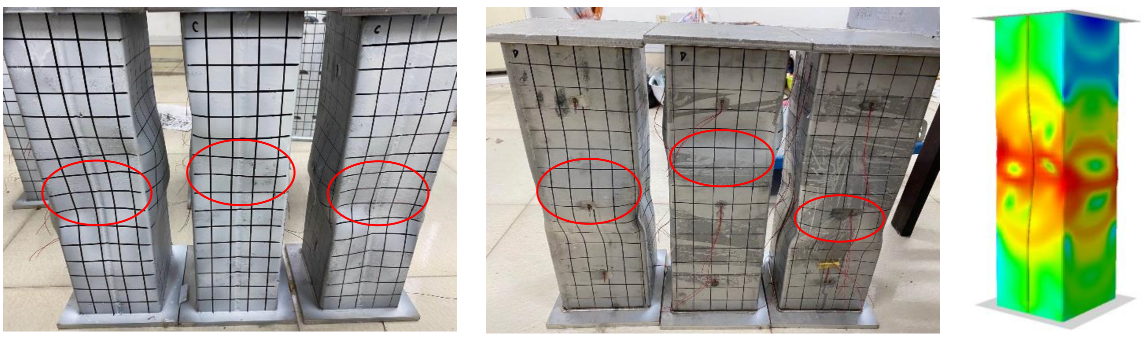

(a) RHS-1 series

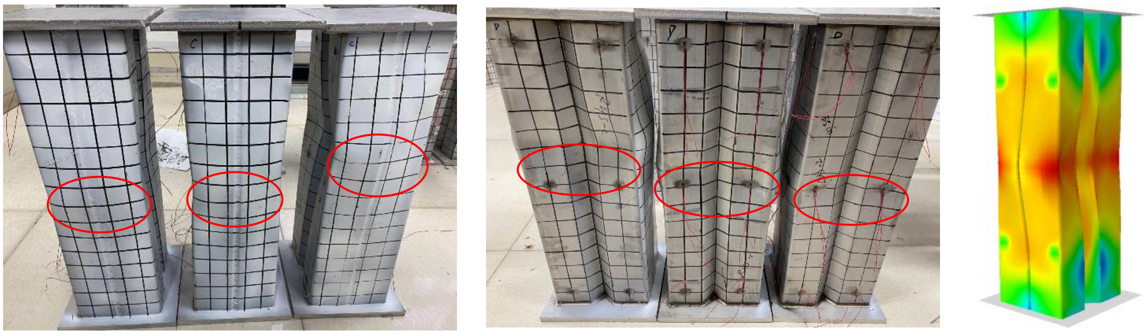

(b) RHS-2 series

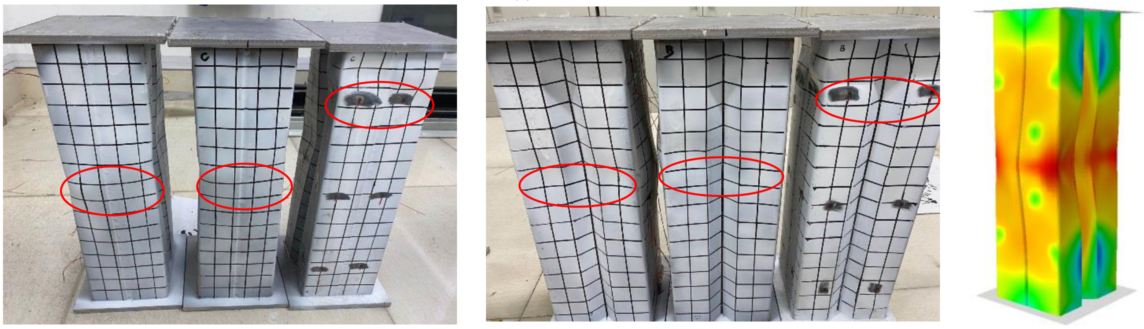

(c) RHS-3 series

Fig. 8 Comparison of failure modes of axial compression short columns

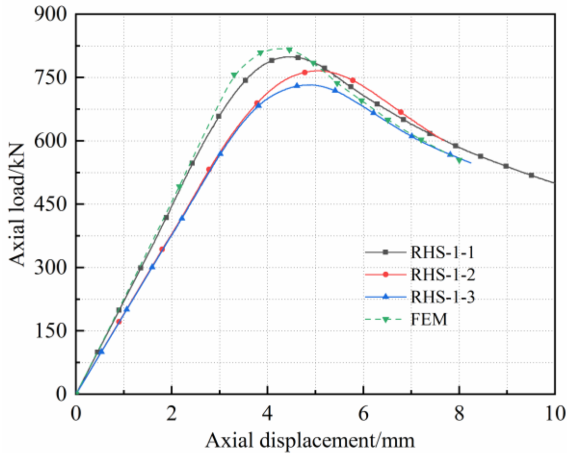

(a) RHS-1 series

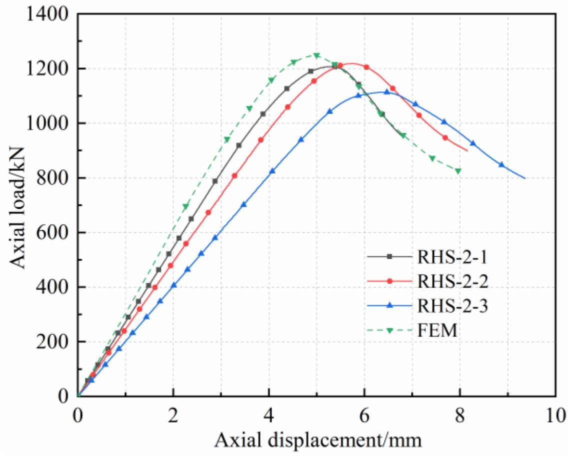

(b) RHS-2 series

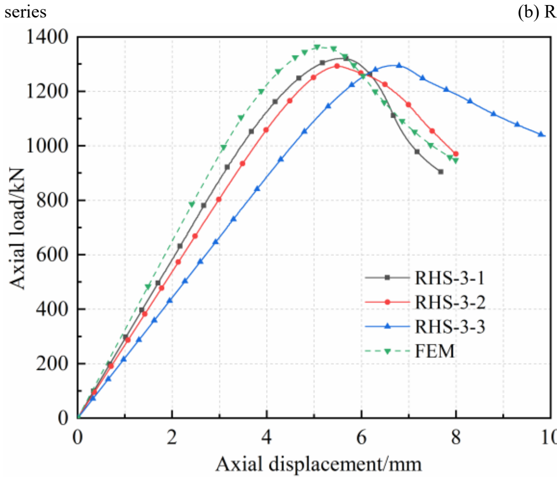

(c) RHS-3 series

Fig. 9 Comparison of axial displacement-load curves

4. Numerical analysis of structural performance and compression-bending capacity calculation

4.1. Analysis of the influence of main parameters of short columns

4.1.1. The influence of the size of V-shaped stiffeners

Ensuring the parameters such as the length of the component being 480mm, the section thickness being 3mm, and the lipped width being 26mm remained unchanged, the depths of the V-shaped stiffeners were 20mm, 23mm, 26mm, 29mm, 32mm, and 35mm respectively, and the angles were 30°, 45°, 60°, 75°, 90°, 105°, and 120° respectively, with a total of 42 components. The ultimate axial compression capacity of all components was obtained through ABAQUS, and the relationship curves between the depth and angle of the V-shaped stiffeners and the ultimate axial compression capacity were plotted, as shown in Fig.10.

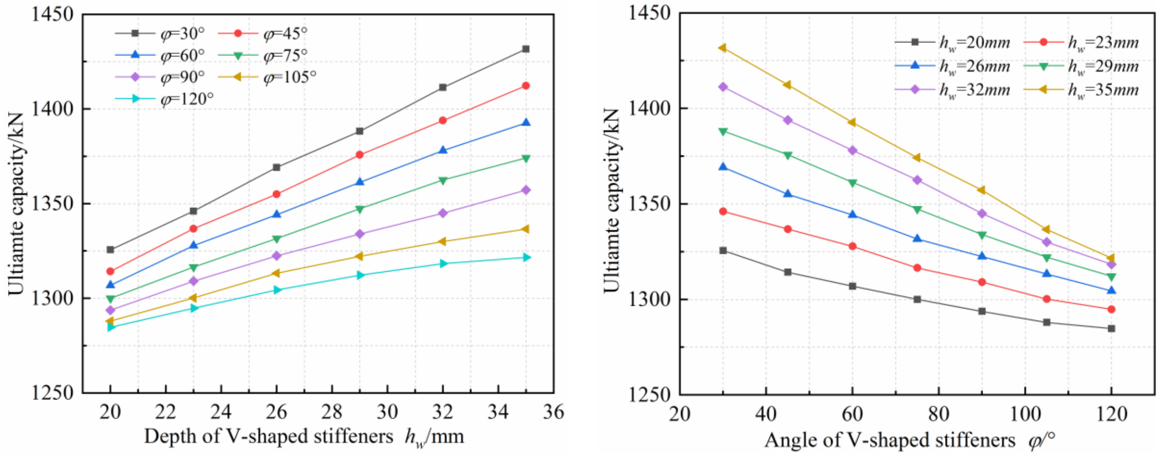

(a) Relationship curve between ultimate capacity and depth of V-shaped stiffeners

(b) Relationship curve between ultimate capacity and angle of V-shaped stiffeners

Fig. 10 Influence of V-shaped stiffeners on ultimate capacity of axial compression columns

It could be seen from Fig.10, the axial compression ultimate bearing capacity of the spliced tubular columns increased linearly with the increase of the depth of the V-shaped stiffeners. When the depth of the V-shaped stiffeners increased from 20 mm to 35 mm, the axial compression ultimate bearing capacity was enhanced by approximately 2.79%-7.41%. On the other hand, the axial compression ultimate bearing capacity decreased linearly with the increase of the angle of the V-shaped stiffeners. Moreover, the smaller the depth of the V-shaped stiffeners was, the gentler the decreasing trend was. For different depths of the V-shaped stiffeners, when the angle of the V-shaped stiffeners increased from 30° to 120°, the axial compression ultimate bearing capacity was reduced by approximately 3.08%-7.79%.

The capacity performance index $N_u/A\sigma_{0.2}$ of the short column was calculated, and the scatter diagram between it and the width-thickness ratio of the V-shaped stiffeners was plotted to further analyze the influence of the V-shaped stiffeners on the axial compression performance of short columns, as shown in Fig.11.

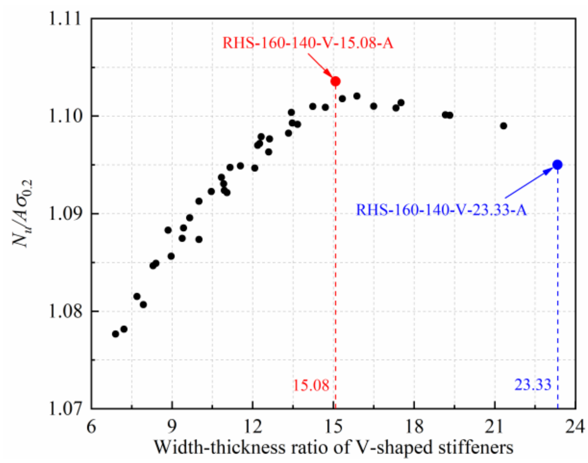

Fig. 11 The scatter diagram of the capacity performance index and the width-thickness ratio

When the width-thickness ratio of the V-shaped stiffeners plate was less than 15.08, the capacity performance index $N_u/A\sigma_{0.2}$ increased with the increase of the width-thickness ratio, and the growth trend gradually slowed down. When the width-thickness ratio was greater than 15.08, the capacity performance index $N_u/A\sigma_{0.2}$ fluctuated slightly with the increase of the width-thickness ratio. When the width-thickness ratio was greater than 19.33, the capacity performance index $N_u/A\sigma_{0.2}$ decreased significantly. The reason was that the width-thickness ratio of the V-shaped stiffener plates was relatively large and exceeded the width-thickness ratios of the web sub-plates and the flange plates. This caused the V-shaped stiffeners to experience local buckling prior to the web and the flange, further leading to a significant reduction in the capacity performance index $N_u/A\sigma_{0.2}$ of the load-bearing capacity. When designing the V-shaped stiffeners, it was recommended that the width-thickness ratio be controlled between 14 and 18, and should not exceed 19.33.

When the width-thickness ratio was 15.08, the capacity performance index $N_u/A\sigma_{0.2}$ reached the maximum, that is, the utilization efficiency of the section and the material reached the highest. Therefore, the width-thickness ratio of all components in the subsequent parameter analysis was controlled to be 15.08, that is, the depth of the V-shaped stiffeners was 32mm and the angle was 90°.

4.1.2. The influence of the height-thickness ratio

According to the regulations on the lipped width in CECS 410: 2015 [29], the optimized setting range of the lipped width was 20-36mm, with a total of 9 components. The ultimate axial compression capacity was obtained through ABAQUS, and the relationship curve between the lipped width and the ultimate axial compression capacity was plotted, as shown in Fig.12.

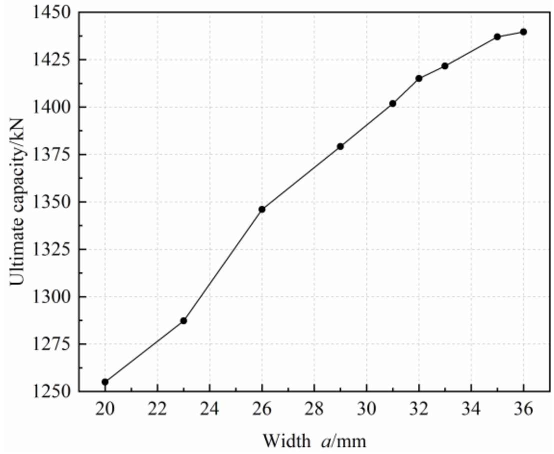

Fig. 12 Effect of lipped width on ultimate capacity of axial compression columns

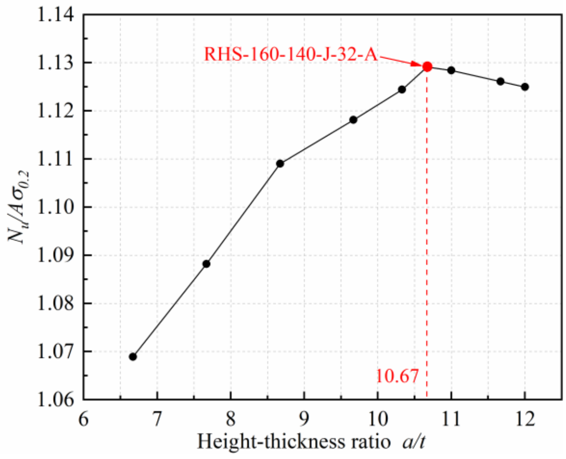

Fig. 13 Point-line diagram of the capacity performance index and height-thickness ratio

The ultimate axial compression capacity increased with the increase of the lipped width, and as the lipped width increased, the growth trend gradually flattened. When the lipped width increased from 20mm to 23mm, 26mm, 29mm, 31mm, 32mm, 33mm, 35mm, and 36mm respectively, the ultimate axial compression capacity of short columns increased by 2.57%, 7.25%, 9.89%, 11.69%, 12.76%, 13.28%, 14.51%, and 14.71% respectively. The capacity performance index $N_u/A\sigma_{0.2}$ was calculated, and the dot-line graph between it and the height-thickness ratio was plotted to further analyze the influence of the lipped part on the axial compression performance, as shown in Fig.13.

When the lipped width was less than 32mm, that is, height-thickness ratio was less than 10.67, the capacity performance index $N_u/A\sigma_{0.2}$ increased with the increase of the height-thickness ratio. When the lipped width was greater than 32mm, that is, the height-thickness ratio was greater than 10.67, as the height-thickness ratio continued to increase, the capacity performance index $N_u/A\sigma_{0.2}$ gradually decreased. When the lipped width was 32mm, that is, the height-thickness ratio was 10.67, the capacity performance index $N_u/A\sigma_{0.2}$ reached the maximum, that is, the utilization efficiency of the section and the material reached the highest.

4.1.3. The influence of the width-thickness ratio

In this section, finite element modeling and calculation were carried out respectively for two short columns of the same height-width ratio but different sizes. The section forms were shown in Fig.14. According to the actual engineering application, the selection range of the section thickness was 1.0mm to 4.0mm, and the corresponding range of the maximum width-thickness ratio (flange width-thickness ratio) was 10.0 to 87.5, with a total of 60 columns.

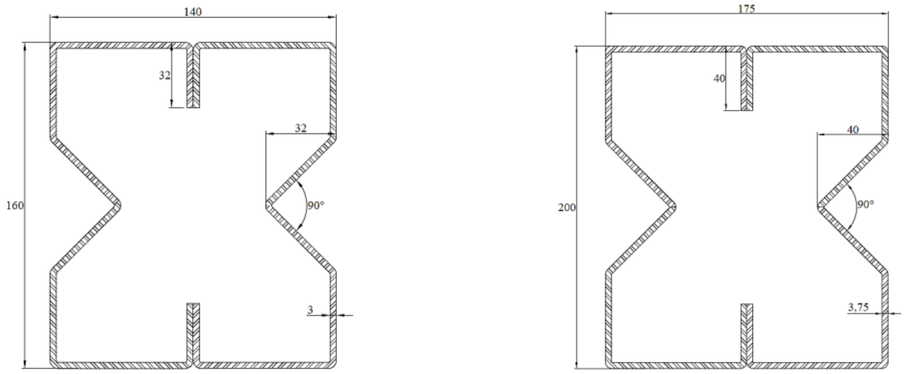

（a）RHS-160-140-A （b）RHS-200-175-A

Fig. 14 Section schematics for plate width-thickness ratio parameter analysis

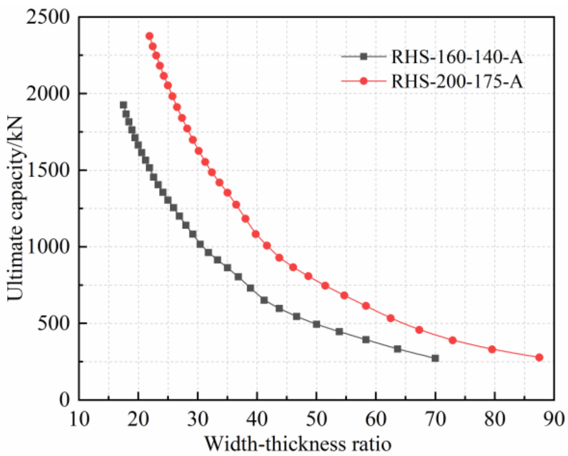

Fig. 15 Relationship curve between ultimate capacity and width-thickness ratio of plates

The ultimate axial compression capacity was obtained through ABAQUS, and the relationship curve between the maximum width-thickness ratio of the plate (flange width-thickness ratio) of the cold-formed thin-walled rectangular tubular column and the ultimate axial compression capacity was plotted, as shown in Fig.15.

When the width-thickness ratio increased, the ultimate axial compression capacity of all short columns gradually decreased, and the decreasing trend gradually flattened with the increase of the width-thickness ratio. When the maximum width-thickness ratio increased from 17.5 to 70, the ultimate axial compression capacity of the RHS-160-140-A series short columns decreased by about 85.9%. When the maximum width-thickness ratio increased from 21.9 to 87.5, the ultimate axial compression capacity of the RHS-200-175-A series short columns decreased by about 88.3%. The scatter diagram N_u/Af_y with the width-thickness ratio according to the most unfavorable plate in the section was drawn, as shown in Fig.16.

For the critical width-thickness ratio limits of stiffened and unstiffened plates, the stipulated values in the Chinese code CECS 410: 2015 were rather conservative and had large differences. In order to make full use of the characteristics of the stainless-steel material and achieve a more economical and reasonable design purpose, take the value of 1 on the ordinate of the fitting curve as the width-to-thickness ratio limit of the compression plate element, and round it to an integer. It was recommended that the critical width-thickness ratio of the stiffened plates be 34, and that of the unstiffened plates be 15.

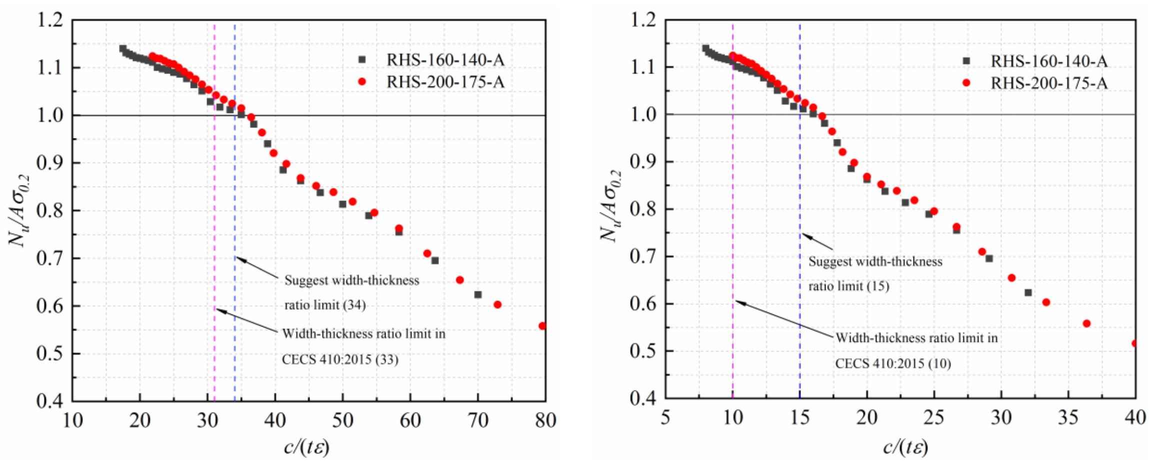

(a) Ribbed components (b) Non-ribbed components

Fig. 16 Recommended critical width-thickness ratio of compressed plates

4.1.4. The influence of the slenderness ratio

At present, the Chinese code stipulated that the allowable slenderness ratio of the axial compression component was 150. Therefore, the length was selected to vary from 480mm to 7200mm, and the variation range of the slenderness ratio was 9.82-147.56, with a total of 33 components. The ultimate axial compression capacity of all components was calculated. The relationship curves between the slenderness ratio and the ultimate axial compression capacity, the relationship curves between the slenderness ratio and the capacity performance index $N_u/A\sigma_{0.2}$ were plotted, as shown in Fig.17 and Fig.18.

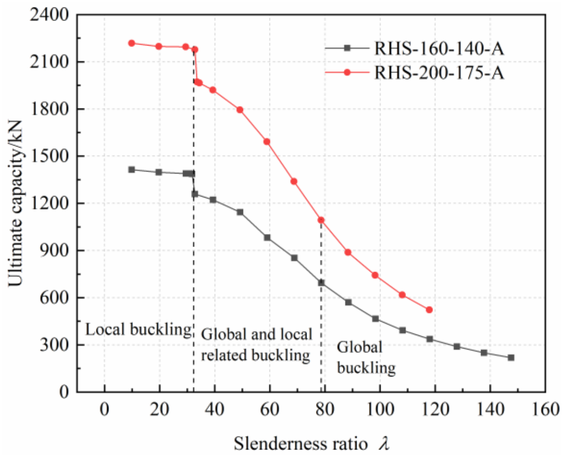

Fig. 17 Relationship curve between ultimate capacity and slenderness ratio

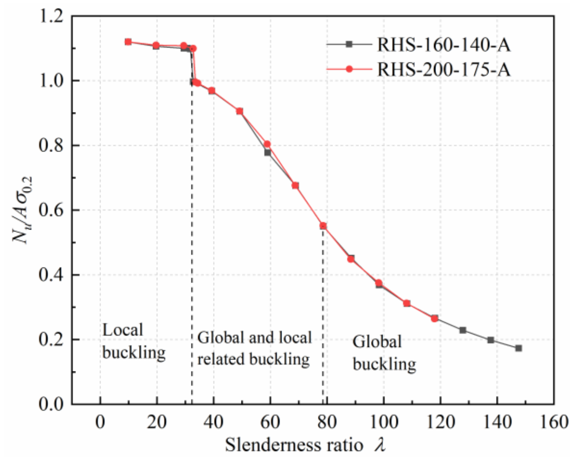

Fig. 18 Relationship curve between the capacity performance index and slenderness ratio

When the slenderness ratio $\lambda \leq 32.74$, the ultimate axial compression capacities were similar, indicating that within this slenderness ratio range, the slenderness ratio had a small influence on the ultimate axial compression capacity, the failure mode was still local buckling. When the slenderness ratio increased from 32.791 to 147.56, the ultimate axial compression capacity of the RHS-160-140-A series components decreased from 1258.31 kN to 218.348 kN, with a reduction of 80.26%. When the slenderness ratio increased from 33.55 to 117.85, the ultimate axial compression capacity of the RHS-200-175-A series components decreased from 1971.34 kN to 522.495 kN, with a reduction of 73.49%. The relationship curves of the ultimate axial compression capacity of different series of components all had inflection points. The slenderness ratio had a significant influence on the ultimate axial compression capacity of the short columns, the failure mode was the overall instability. When the slenderness ratio $\lambda \leq 32.74$, because the failure mode was local buckling, the capacity performance index $N_u/A\sigma_{0.2}$ was close. When the slenderness ratio $\lambda > 33.55$, because the failure mode was overall buckling, the capacity performance index $N_u/A\sigma_{0.2}$ gradually decreased as the slenderness ratio increased, and as the slenderness ratio increased, the decreasing trend gradually flattened.

4.2. Analysis of the influence of main parameters of compression-bending short columns and median long columns

4.2.1. The influence of the relative eccentricity of the load

In practical engineering applications, the compression-bending members were mostly in the state of eccentric compression around the strong axis. Therefore, in this section, only the finite element parametric analysis of spliced tubular columns under eccentric compression around the strong axis would be carried out. And the analysis will be conducted with two commonly used member lengths (900 mm and 3000 mm) in practical engineering. Ensuring that the section thickness was 3mm, the width-thickness ratio of the V-shaped stiffeners plate was 15.08, and the height-thickness ratio was 10.67 remained unchanged, only by changing the eccentricity of the load, the influence of the relative eccentricity of the load on the compression-bending performance of the cold-formed thin-walled rectangular high-strength stainless-steel spliced tubular columns was studied. The load eccentricities were respectively set to 8mm, 16mm, 32mm, 64mm, 96mm, 128mm, and 160mm, and the corresponding relative eccentricities of the load were respectively 0.1, 0.2, 0.4, 0.8, 1.2, 1.6, and 2.0. And two commonly used component lengths (900mm, 3000mm) in actual engineering were selected, with a total of 14 components. The ultimate compression-bending stability capacity under different relative eccentricities of the load was obtained, and the relationship curve was plotted, as shown in Fig.19.

When the slenderness ratio $\lambda_x = 14.81$ and $\lambda_x = 48.79$, as the relative eccentricity of the load increased, the ultimate compression-bending capacity gradually decreased, and as the relative eccentricity of the load increased, the decreasing trend of the ultimate capacity gradually flattened. When the relative eccentricity of the load increased from 0.1 to 2.0, the ultimate compression-bending capacity eccentrically compressed around the strong axis decreased by 72.14% and 69.01% respectively, indicating that the relative eccentricity of the load had a significant influence on the ultimate capacity of the compression-bending column.

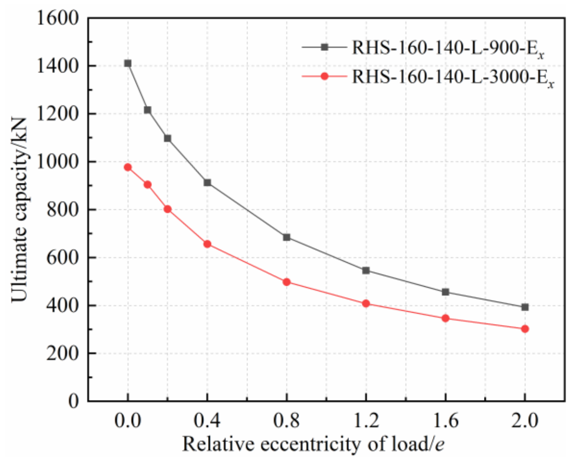

Fig. 19 Relationship curve between relative eccentricity of load and ultimate capacity

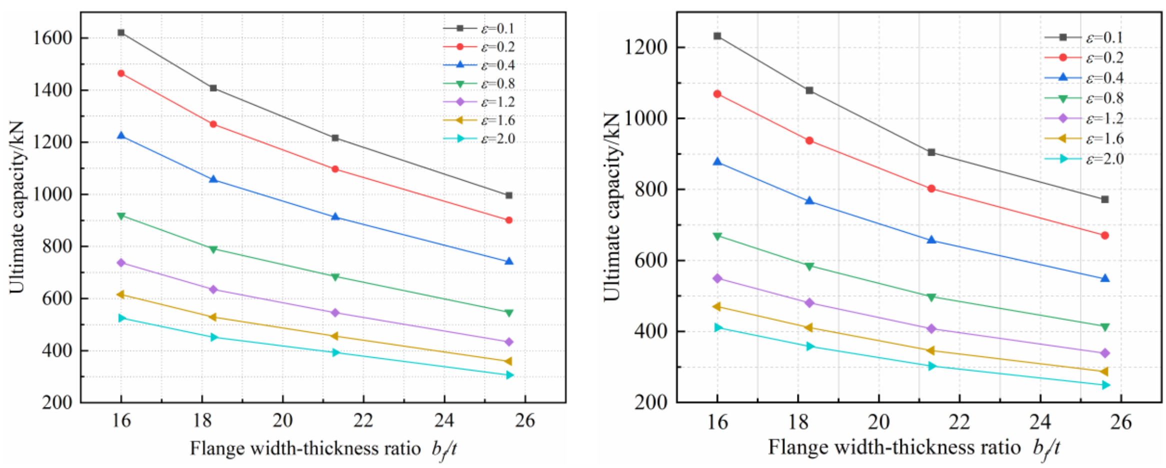

(a) 900mm eccentric compression component around the strong axis (a) 3000mm eccentric compression component around the strong axis

Fig. 20 Relationship curve between width-thickness ratio and ultimate compression-bending capacity

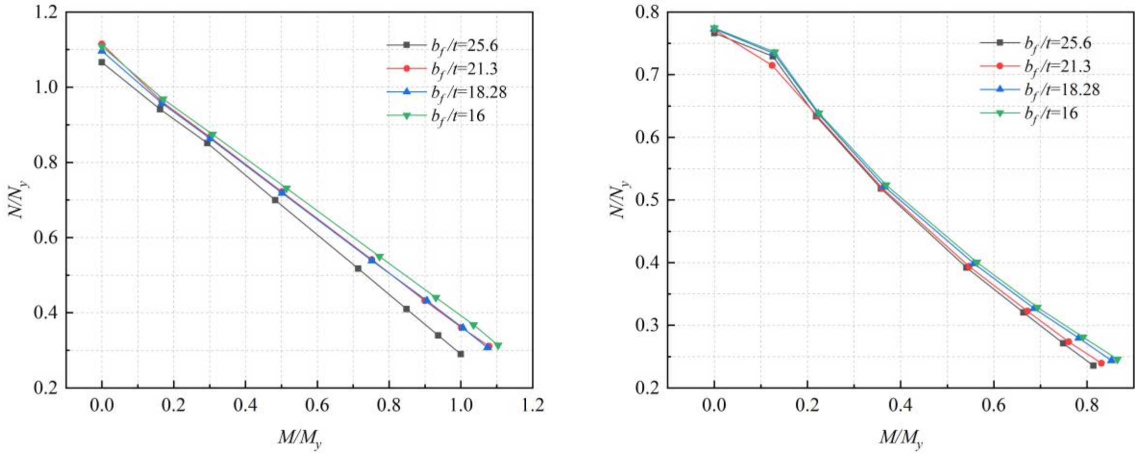

(a) RHS-160-140-L-900-Ex series (b) RHS-160-140-L-3000-Ex series

Fig. 21 Stable capacity N-M correlation curve of spliced components

4.2.2. The influence of the width-thickness ratio

The section thicknesses were 2.5mm, 3mm, 3.5mm, and 4.0mm, that is, the maximum width-thickness ratio of the plate (flange width-thickness ratio) was 25.6, 21.3, 18.28, and 16. The analysis was carried out with two commonly used component lengths (900mm, 3000mm), with a total of 56 components. The ultimate compression-bending stability capacity of the cold-formed thin-walled components with different section thicknesses was obtained, as shown in Fig.20. Considering that the section thickness had a direct influence on the cross-sectional area, in order to eliminate the influence of the cross-sectional area, the finite element calculation results were sorted and plotted into the axial force-bending moment correlation curve, as shown in Fig.21. As the bending moment M increased, the spacing of the N-M curve under the same abscissa gradually increased, indicating that as the relative eccentricity of the load increased, the influence of the width-thickness ratio on the ultimate compression-bending stability capacity gradually strengthened. In other words, as the width-thickness ratio of the flange increased, the downward trend of the N-M curve gradually became gentler, also represented the influence of the width-thickness ratio on the ultimate compression-bending stability capacity gradually strengthened.

4.2.3. The influence of slenderness ratio

Ensuring that the section thickness was 3mm, the width-thickness ratio of the V-shaped stiffeners plate was 15.08, and the height-thickness ratio was 10.67 remained unchanged, only by changing the component length, the influence of the slenderness ratio on the compression-bending performance of the cold-formed thin-walled high-strength stainless-steel spliced was studied. The component length varied from 900mm to 6000mm, and the corresponding variation range of the slenderness ratio was 14.81 to 98.73, with a total of 35 components. The compression-bending stability capacity with different slenderness ratios was obtained, and the relationship curve between the slenderness ratio and the compression-bending stability capacity was plotted, as shown in Fig.22.

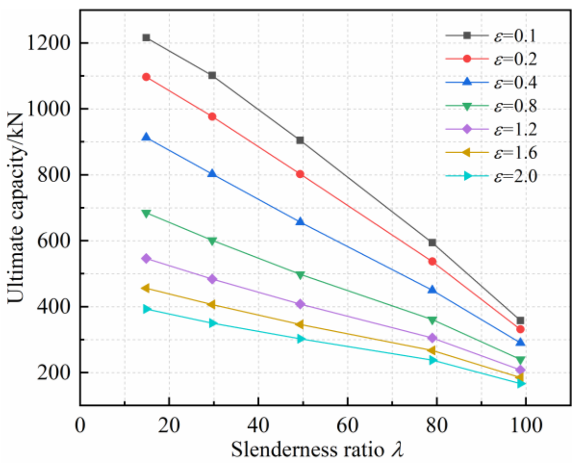

Fig. 22 Relationship curve between ultimate capacity and slenderness ratio

With the slenderness ratio increased, the compression-bending stability capacity decreased significantly, and as the relative eccentricity of the load increased, the decreasing trend flattened. Longitudinally comparing the compression-bending stability capacities of components with different relative eccentricities of the load, it could be found that as the slenderness ratio increased, the influence of the relative eccentricity of the load on the compression-bending stability capacity gradually decreased. The reason was that as the slenderness ratio increased, the overall stiffness significantly attenuated, and the final failure mode was mainly overall buckling.

4.3. Recommendation of compression-bending capacity calculation formula

According to the calculation formulas for the compression-bending bearing capacity in the Chinese code CECS 410:2015 [29] and the American code AISI S100-16 [30], the ultimate compression-bending stability bearing capacity of the spliced tubular columns was calculated respectively, as shown in Fig.23. Then, a comparative analysis was carried out between the calculation results of the codes and those of the finite element simulation. The average value of the ratio N_{FEA}/N_u between the finite element simulation result N_{FEA} and the calculation result N_u of the Chinese code was 1.127, with a standard deviation of 0.151 and a coefficient of variation of 0.134. The average value of the ratio N_{FEA}/N_d between the finite element simulation result N_{FEA} and the calculation result N_d of the American code was 1.133, with a standard deviation of 0.115 and a coefficient of variation of 0.102. Overall, the calculation results of the American code, which adopted the load and restraint factor design method, were more accurate than those of the Chinese code, which adopted the effective width method. However, compared with the finite element simulation results, the calculation results of both the Chinese and American codes had relatively large differences, a high degree of dispersion, and the calculation results of some spliced tubular columns tended to be unsafe.

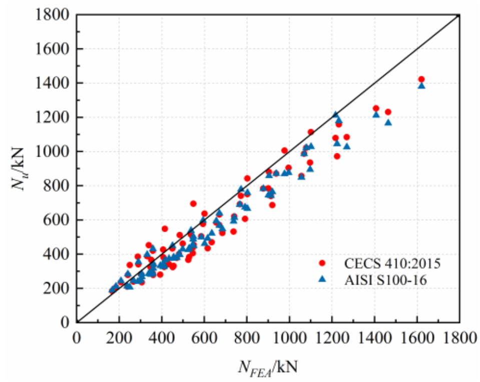

Fig. 23 Scatter diagram of compression-bending capacity of spliced tubular columns calculated by Chinese and American codes

Made appropriate modifications to the calculation formula for the ultimate bending-compression stability bearing capacity proposed in the Chinese code, so that it could be applicable to the new high-strength stainless-steel spliced tubular compression-bending columns proposed in this paper. The Chinese code CECS410: 2015 stipulated that for the strength of compression-bending components, it could be calculated according to the Eq.(1):

$$\sigma = \frac{N}{A_{en}} \pm \frac{M_x}{W_{enx}} \pm \frac{M_y}{W_{eny}} \le f \tag{1}$$

Where: N -Axis compressive pressure;

A_{en} -Effective cross-section area of the component;

M_x, M_y -The bending moment around the main axes x-axis and y-axis;

W_{enx}, W_{eny} -The effective net section modulus for the main axes x-axis and y-axis.

When calculating the stability of compression-bending components, when within the plane of the bending moment action, it can be calculated according to the Eq.(2) and Eq.(3):

$$\frac{N}{\varphi_x A_e}+\frac{\beta_m M}{\left(1-\varphi_x\frac{N}{N'_E}\right)W_e}\le f \quad (2)$$

$$N'_E=\frac{\pi^2 E_0 A}{1.165\lambda^2} \quad (3)$$

Where, β_m -Equivalent bending moment coefficient, $\beta_m = 1.0$;

M -Calculating the bending moment;

N'_E -Euler critical load;

W_e -The effective section modulus of the maximum compression edge in the bending plane.

When the bending moment is outside the plane of action, the stability of the compression-bending component can be calculated according to the Eq.(4):

$$\frac{N}{\varphi_y A_e}+\frac{\eta M}{\varphi_{bx} W_{ex}}\le f \quad (4)$$

Where, φ_y -Overall stability coefficient of the bending component out of bending moment;

η -Cross section influence coefficient, for the rectangular section column, $\eta = 0.7$;

φ_{bx} -Overall stability coefficient of the bending component, for the rectangular section, because of its large torsional stiffness, $\varphi_{bx} = 1.0$.

Referring to the form of the calculation formula of the in-plane compression-bending capacity of ordinary steel, the calculation formula of the compression-bending capacity in the Chinese code was modified. According to the finite element simulation results, the least square method was used for multiple linear regression fitting, and the modified formula was obtained as Eq. (5) and Eq. (6):

$$\frac{N}{\varphi_x A_e}+\frac{\beta_m M}{\gamma\left(1-\varphi_x\frac{N}{N'_E}\right)W_e}\le f \quad (5)$$

$$\gamma = 1.245+1.97\times10^{-4}\varepsilon^{13.7} \quad (6)$$

As for the calculation formula of the compression-bending capacity outside the plane of the bending moment action, since the rectangular tubular column proposed was not a completely rectangular section, and according to the finite element simulation results, the section influence coefficient was adjusted and taken as $\eta = 0.85$. According to the modified calculation formula of the compression-bending capacity in the Chinese code, the calculation of the cold-formed thin-walled rectangular compression-bending column was carried out. The results were compared with the finite element simulation results, as shown in Fig.24, where N'_u was the calculated result after the modification of the Chinese code.

It could be concluded that the average value of the ratio N_{FEA}/N'_u was 1.034, the standard deviation was 0.022, the coefficient of variation was 0.021, and the maximum difference was only 8.5%. This indicated that the calculated results of the modified compression-bending capacity were very close to the finite element simulation results and were feasible for calculating the ultimate compression-bending stability capacity of the cold-formed thin-walled rectangular tubular column.

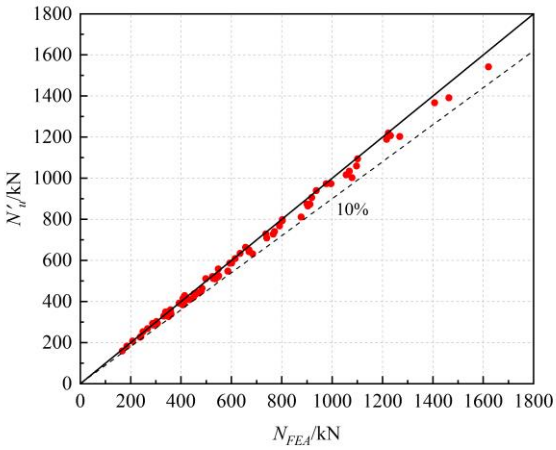

Fig. 24 Compression-bending capacity calculated by the Chinese code after revision

5. Conclusions

This paper designed a cold-formed thin-walled rectangular high-strength stainless-steel spliced tubular columns to meet the requirements of the marine steel structure. Experiment of axial compression short columns, finite element analysis of axial compression short columns, compression-bending short columns and median long columns was carried out. The main conclusions were as follows:

(1) Two stainless-steel lipped channels spliced into rectangle columns effectively enhanced the stable capacity of short columns. Compared with the RHS-1 series short columns, the capacity of the RHS-2 series increased by 46.15%, the capacity of the RHS-3 series increased by 55.38%. The V-shaped stiffeners and the straight ribs played a full stiffening role in the axial compression test, improving the final buckling mode of the short columns and reflecting the efficiency of the spliced section.

(2) The main failure mode of the axial compression short columns was the local buckling failure. The V-shaped stiffeners changed the position where local buckling occurred from the long side to the short side, and the two sub-plates on the long side buckled respectively. Optimizing the length of the straight ribs formed by the lipped edge changed the buckling half-wave of the short side from one buckling half-wave to two buckling half-waves.

(3) For rectangular spliced axial compression short columns, the V-shaped stiffeners and the slenderness ratio had a great influence on failure modes. When the depth of the V-shaped stiffener was 32 mm and the angle was 90°, the section performance was optimal. When the slenderness ratio was in the range of 33.55-147.56, the overall buckling failure occurred.

(4) For rectangular spliced compression-bending short columns and median long columns, the eccentricity ratio and the slenderness ratio had a great influence on failure modes. When the eccentricity ratio increased from 0.1 to 2.0, the ultimate compression-bending capacity decreased by 72.14% and 69.01% respectively. When the slenderness ratio was in the range of 14.81-98.73, the compression-bending stability capacity decreased significantly with the increase of the slenderness ratio.

(5) A modified calculation formula for the ultimate capacity of compressio n-bending columns was proposed, it can be used to expand the application sco pe of Chinese code and American code, with high accuracy.

In the future, experimental research on median long spliced tubular columns is recommended. Moreover, only V-shaped stiffeners are installed in the middle of the web to improve the axial compression bearing capacity, more composite section forms can be explored to promote the application of stainless-steel in load-bearing members in offshore steel structures.

Reference

[1] M. Ahmed, R.I. Shahin, S.A. Yehia, M. Emara, V.I. Patel, Q.Q. Liang, Nonlinear analysis of square steel-reinforced concrete-filled steel tubular short columns considering local buckling, Struct. Concr. (2023) 69-84.

[2] Y.F. Yang, M. Liu, F. Fu, Experimental and numerical investigation on the performance of three-legged CFST latticed columns under lateral cyclic loadings, Thin-Walled Struct. 132 (2018) 176-194.

[3] M. Ahmed, S.A. Yehia, R.I. Shahin, M. Emara, V.I. Patel, Q.Q. Liang, Numerical simulation and design of circular steel-reinforced concrete-filled steel tubular short columns under axial loading, Mag. Concr. Res. (2023) 1-44.

[4] Q.X. Wu, Z.K. Xu, H.H. Yuan, Z.Q. Qin, Experimental study of axial compressive performance of UHPC-encased CFST composite stub columns, J. Build. Struct. 44 (12) (2023) 183-193.

[5] J. Cai, J. Pan, X. Li, Behavior of ECC-encased CFST columns under axial compression, Eng. Struct. 171 (2018) 1-9.

[6] M.F. Hassanein, V.I. Patel, M. Elchalakani, H.T. Thai, Finite element analysis of large diameter high strength octagonal CFST short columns, Thin-Walled Struct. 123 (2018) 467-482.
[7] P. Ayough, N.H.R. Sulong, Z. Ibrahim, Analysis and review of concrete-filled double skin steel tubes under compression, Thin-Walled Struct. 148 (2020) 106495.
[8] Z.W. Shao, X.X. Zha, C.Y. Wan, Design method of fire-resistance capacity of reinforced-concrete-filled steel tube column under axial compression, Fire Saf. J. 129 (2022) 103572.
[9] K.U. Ukanwa, G.C. Clifton, J.B. Lim, S.J. Hicks, U. Sharma, A. Abu, Simple design procedure for concrete filled steel tubular columns in fire, Eng. Struct. 155 (2018) 144-156.
[10] A.P.C. Duarte, B.A. Silva, N. Silvestre, J. de Brito, E. Julio, J.M. Castro, Tests and design of short steel tubes filled with rubberised concrete, Eng. Struct. 112 (2016) 274-286.
[11] Q.H. Tan, L. Gardner, L.H. Han, T.Y. Song, Fire performance of steel reinforced concrete-filled stainless steel tubular (CFSST) columns with square cross-sections, Thin-Walled Struct. 143 (2019) 106197.
[12] E. Ellobody, Nonlinear behavior of concrete-filled stainless steel stiffened slender tube columns, Thin-Walled Struct. 45(2007) 259-273.
[13] Z.M. Lai, A.H. Varma, Noncompact and slender circular CFT members: Experimental database, analysis, and design, J. Constr. Steel Res. 101 (2014) 455-468.
[14] F. Aslani, B. Uy, Z. Tao, Predicting the axial load capacity of high-strength concrete filled steel tubular columns, Steel Compos. Struct. 19 (2015) 967-993.
[15] W.F. Zhang, L. Gardner, M.A. Wadee, On the uniform torsional rigidity of square concrete-filled steel tubular (CFST) sections, Struct. 43 (2022) 249-2521.
[16] Z. Tao, B. Uy, Analysis and design of concrete-filled stiffened thin-walled steel tubular columns under axial compression, Thin-Walled Struct. 47 (2009) 1544-1556.
[17] J.G. Wei, X. Luo, Z.C. Lai, B.C. Chen, Experimental study on axial compressive behavior of circular UHPC filled high-strength steel tube short columns, J. Struct. Eng. 41 (2020) 16-28.
[18] S. Chen, R. Zhang, L.J. Jia, J.Y. Wang, P. Gu, Structural behavior of UHPC filled steel tube columns under axial loading, Thin-Walled Struct. 130 (2018) 550-563.
[19] Z. Xu, Study on the flexion capacity of reinforced cold-bent thin-walled C-shaped steel axial compression component , Huazhong University of Science and Technology, 2019. (in Chinese)
[20] D.A. Padilla-Llano, C.D. Moen, M.R. Eatherton, Cyclic axial response and energy dissipation of cold-formed steel framing components, Thin-Walled Struct. (2014) 95-107.
[21] Y. Lu, T. Zhou, W. Li, et al, Experimental investigation and a novel direct strength method for cold-formed built-up I-section columns, Thin-Walled Struct. 112 (2017) 125-139.
[22] H.X. Niu, A.H. Han, Y.J. Hou, Numerical analysis of cold-formed thin-walled C-shaped steel columns in different stiffening forms, Low temperature building technology, 44 (2022) 85-88. (in Chinese)
[23] B. Young, J. Chen, Design of cold-formed steel built-up closed sections with intermediate stiffeners, J. Struct. Eng. 134 (2008) 727-737.
[24] W. Reyes, A. Guzmán, Evaluation of the slenderness ratio in built-up cold-formed box sections, J. Constr. Steel Res. 67 (2011) 929-935.
[25] I. Georgieva, L. Schueremans, L. Vandewalle, et al. Numerical study of built-up double-Z components in bending and compression, Thin-Walled Struct. 60 (2012) 85-97.
[26] J. Zhang, B. Young, Compression tests of cold-formed steel I-shaped open sections with edge and web stiffeners, Thin-Walled Struct. 52 (2012) 1-11.
[27] F. Liao, H. Wu, R. Wang, et al. Compression test and analysis of multi-limbs built-up cold-formed steel stub columns, J. Constr. Steel Res. 128 (2017) 405-415.
[28] H.X. Li, Experimental study on cold-formed thin-walled rectangular tubular stub columns of assembled stainless-steel under axial compression, Nanjing Tech University, 2020. (in Chinese)
[29] Technical specification for stainless-steel structures: CECS410: 2015, China Planning Press, Beijing, 2015 (in Chinese).
[30] AISI-S100-2016, North American cold-formed steel specification, American Iron and Steel Institute, 2016.